Orthogonal Coded Active Illumination for Millimeter Wave, Massive-MIMO Computational Imaging With Metasurface Antennas

Queen's University Belfast - Research Portal:
Link to publication record in Queen's University Belfast Research Portal

Orthogonal Coded Active Illumination for Millimeter Wave, Massive-MIMO Computational Imaging with Metasurface Antennas

Andreas Pedross-Engel, *Senior Member, IEEE,* Daniel Arnitz, *Member, IEEE,* Jonah N. Gollub, *Member, IEEE,*
Okan Yurduseven, *Senior Member, IEEE,* Kenneth P. Trofatter, Mohammadreza F. Imani, *Member, IEEE,*
Timothy Sleasman, *Student Member, IEEE,* Michael Boyarsky, *Student Member, IEEE,*
Xiaojie Fu, *Student Member, IEEE,* Daniel L. Marks, David R. Smith, *Member, IEEE,*
and Matthew S. Reynolds, *Senior Member, IEEE*

Abstract—Emerging metasurface antenna technology enables flexible and low cost massive multiple-input multiple-output (MIMO) millimeter-wave (mmW) imaging for applications such as personnel screening, weapon detection, reconnaissance, and remote sensing. This work proposes an orthogonal coded active illumination (OCAI) approach which utilizes simultaneous, mutually orthogonal coded transmit signals to illuminate the scene being imaged. It is shown that OCAI is robust to code amplitude and code phase imbalance introduced by imperfect transmitter (TX) and receiver (RX) hardware, while also mitigating common impairments of low cost direct-conversion receivers, such as RX self-jamming and DC offsets. The coding gain offered by this approach improves imager signal to noise ratio (SNR) performance by up to 15 dB using codes of symbol length 32. We present validation images of resolution targets and a human-scale mannequin, obtained with a custom massive-MIMO mmW imager having 24 simultaneous TX and 72 simultaneous RX operating in the K-band (17.5 GHz to 26.5 GHz). The imager leverages both spatial coding via frequency diverse metasurface antennas, and temporal coding via OCAI of the scene.

Index Terms—Computational imaging, Imaging systems, metamasurface antennas, millimeter wave (mmW), MIMO, orthogonal codes.

I. INTRODUCTION

MILLIMETER-WAVE (mmW) imaging has many applications such as reconnaissance, remote sensing [1]–[3], autonomous robotics [4], [5], non-destructive testing [6], security screening [7], and concealed weapon detection [8]. In active mmW imaging, the region of interest (ROI) in a scene is illuminated by one or more transmitters, while the scattered energy from the scene is spatially sampled. Many active imagers leverage mechanical motion of an antenna array to form a synthetic aperture radar (SAR) image [1], [9]. Other active imagers use phased arrays such as active electronically scanned arrays (AESAs) [10]. Phased arrays exploit a large number of antenna elements to form a large, spatially sampled aperture [5], [11].

These existing approaches often have significant disadvantages. SAR acquisition time is often slow due to the required mechanical motion, which may lead to motion blur for close-in, fast moving targets. Phased array and AESA based imagers are often expensive, power hungry, and complex due to the large amount of RF hardware such as transmitters (TX), receivers (RX), and phase shifters needed.

Recent work has focused on reducing the cost and complexity of mmW imagers using computational imaging techniques that exploit sparse apertures formed from metasurface antennas (MSAs) [12]–[14]. Metasurface antennas typically consist of a waveguide fed dense array of sub-wavelength unit cells. An alternative MSA approach is the frequency-diverse chaotic cavity aperture with sub-wavelength irises [15]–[17]. MSAs can generate frequency-diverse chaotic beam patterns which sparsely sample the ROI and enable compressive imaging. As these antennas can be manufactured using established, low-cost manufacturing processes, the cost and design cycle for metasurface based imagers can be advantageous compared to existing approaches [15], [16].

To improve ROI size and achievable resolution, multiple spatially distributed TXs and RXs can be used to obtain a large imager aperture comprised of multiple MSAs. To minimize motion blur due to a moving scene, data acquisition time is critical. The preferred solution is to exploit multiple-input multiple-output (MIMO) processing to operate all TXs and and RXs simultaneously. However, simultaneous TX and RX
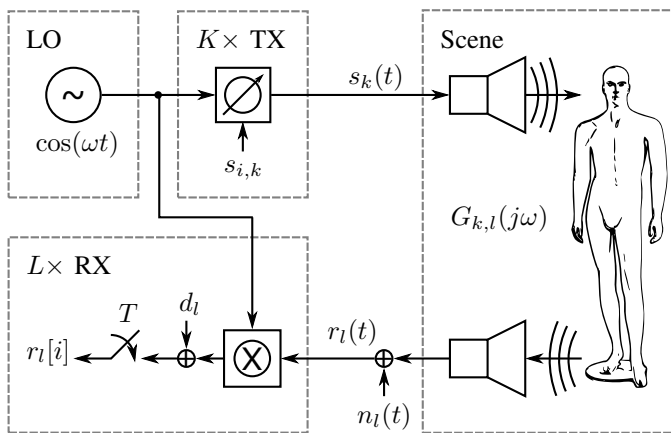
Fig. 1. Block diagram of one TX/RX pair in the MIMO system, including a single oscillator (LO), K TX channels with phase modulators, the imaged scene, and L RX channels.

operation requires the ability to distinguish the signals from different TXs at each receiver, so the TX signals must be somehow separable.

In this work, an orthogonal coded active illumination (OCAI) approach for massive MIMO mmW imaging is proposed which exploits balanced, binary orthogonal codes to separate TX signals at the receivers, while simultaneously mitigating RX self-jamming and DC offset impairments often found in mmW imagers using low cost direct-conversion receivers [18]. We show that the OCAI coding is insensitive to code amplitude and code phase imbalance, and the coding gain leads to an increase in SNR performance by up to 15 dB for codes with length of 32 symbols.

This work is organized as follows: In Section II, the OCAI system model for MIMO imaging is derived. Section III presents numerical simulations needed to analyze the OCAI performance for different code parameters, non-ideal code realizations, and undesired receiver DC offsets. In Section IV, an overview of the prototype K-band (17.5-26.5 GHz) mmW massive MIMO imager hardware is provided. Section V gives an overview of the image reconstruction problem. Image reconstructions of a resolution target and a human scale mannequin obtained from OCAI-based MIMO measurements are presented in Section VI, followed by conclusions.

II. SIGNAL MODELS FOR MIMO IMAGING

A. Illumination with a Single Transmitter

At a high level, the goal of active radio frequency (RF) imaging is to estimate the reflectivity coefficient distribution of a ROI in a scene, given measured backscatter responses between K TXs and L RXs. A scene is assumed to be comprised of N hypothesized point scatters with complex reflectivity $\{\rho_n\}$. The scene is a linear system, so the backscatter frequency response $G_{k,l}(j\omega)$ between the kth TX and lth RX (see Fig. 1) is given as

$$G_{k,l}(j\omega) = \sum_{n=1}^{N} \rho_n \alpha_{k,l,n}(j\omega) e^{-j\omega\tau_{k,l,n}}, \qquad (1)$$

where $k \in \{1, \ldots, K\}$, $l \in \{1, \ldots, L\}$, $\alpha_{k,l,n}(j\omega)$ represents the round-trip path loss and antenna gain, $j = \sqrt{-1}$, and $\tau_{k,l,n}$ is the round-trip propagation delay between the kth TX, lth RX, and the nth point scatter.

Many imaging radars use frequency chirped pulses [19] as the excitation signal, but various ultra-wideband (UWB) signals [20] are also used. For relatively slow varying scenes, stepped frequency modulated continuous wave (stepped-FM) signals [21] are advantageous. In the stepped-FM scheme, each TX emits a sequence of constant amplitude tones, having different frequencies. These tones illuminate the scene and enable a sampled measurement of the frequency response $G_{k,l}(j\omega)$ one frequency step at a time. Given a single tone

$$s_k(t) = \Re\left\{e^{+j\omega t}\right\} \qquad (2)$$

emitted by the kth TX, the received signal at the lth RX can be represented as

$$r_l(t) = \Re\left\{G_{k,l}(j\omega)e^{+j\omega t}\right\} + n_l(t), \qquad (3)$$

where t is time, $\Re\{\cdot\}$ is the real operator, and $n_l(t)$ is measurement noise. After down-conversion and sampling with sampling period T, the received signal is given by

$$r_l[i] = G_{k,l}(j\omega) + d_l + \nu_l[i], \qquad (4)$$

where $i \in \mathbb{N}$ is the sampling index, d_l is a DC offset or RX self-jamming introduced by non-ideal down-converters [18], and $\nu_l[i]$ is complex valued measurement noise. Hence, $r_l[i]$ gives an estimate of the respective frequency response $G_{k,l}(j\omega)$, assuming mitigation of d_l [18].

B. Illumination with Multiple Transmitters

To measure the frequency response between multiple TX-RX pairs at the same time, the transmit signals must be mutually orthogonal to permit each transmitter's contribution to be separated from all others. One way to achieve this is by introducing orthogonal codes as a lower frequency (kHz to MHz) modulation, such as a phase shift keying (PSK) modulation, of the (GHz) stepped-FM tones. While the coded modulation inherently introduces some bandwidth to the illuminating TX signal, practical modulation rates (kHz to MHz) are e.g. 10^{-5} lower than the carrier frequency (GHz). Therefore, any frequency dependence in the scene will not be visible even with modulated illumination.

The transmitted signal from the kth TX, using a code of length M, can be represented as

$$s_k(t) = \Re\left\{e^{+j\omega t} \sum_{i=0}^{M-1} s_{i,k}\, \text{rect}_T\, (t - iT)\right\}, \qquad (5)$$

where $s_{i,k} \in \{-1, +1\}$ is the ith binary code symbol of the kth transmitter, and $\text{rect}_T(t)$ is a unit rectangle over the code symbol period $0 \leq t < T$. The received signal of the lth RX is therefore given as

$$\begin{aligned} r_l(t) = \sum_{k=1}^{K} \Re\Bigg\{ &G_{k,l}(j\omega)e^{+j\omega t} \sum_{i=0}^{M-1} s_{i,k}\, \text{rect}_T\, (t - iT)\Bigg\} \\ &+ n_l(t). \end{aligned} \qquad (6)$$
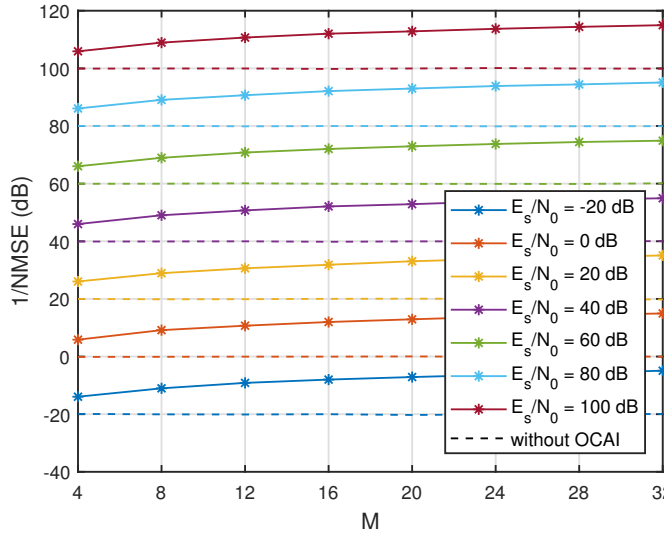
Fig. 2. Comparison of the 1/NMSE performance with and without OCAI as a function of code length M and different E_s/N_0 levels, for $K = 3$ transmitters.
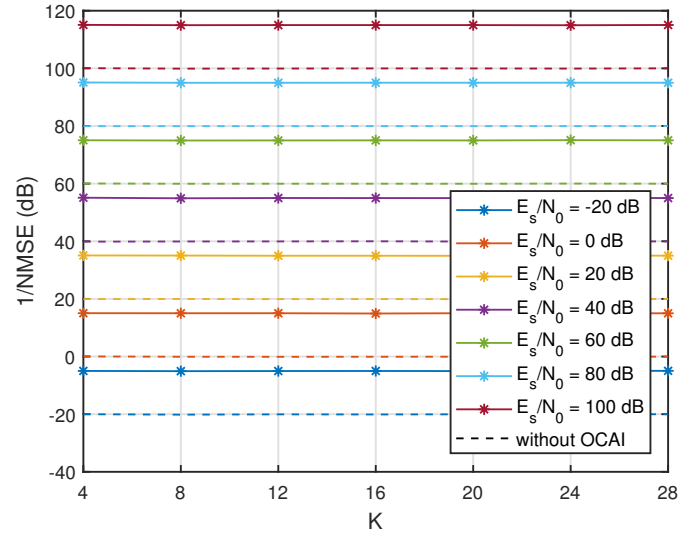

Fig. 3. Comparison of the 1/NMSE performance with and without OCAI as a function of the number of TXs K and different E_s/N_0 levels.

After down-conversion and sampling, the received signal is

$$r_l[i] = \sum_{k=1}^{K} G_{k,l}(j\omega)s_{i,k} + d_l + \nu_l[i]. \tag{7}$$

Concatenating the M received samples from the lth RX in a vector $\mathbf{r}_l = [r_l[0] \ r_l[1] \ \dots \ r_l[M-1]]^T$, where $(\cdot)^T$ is the transpose operator, leads to the linear vector equation

$$\mathbf{r}_l = \mathbf{S}\mathbf{g}_l + d_l\mathbf{1} + \boldsymbol{\nu}_l, \tag{8}$$

where each matrix element $[\mathbf{S}]_{(i+1),k} = s_{(i+1),k}$, $[\mathbf{g}_l]_k = G_{k,l}(j\omega)$, $\mathbf{1}$ is a vector of all ones, and $[\boldsymbol{\nu}_l]_{(i+1)} = \nu_l[i]$.

The TX codes are chosen to be mutually orthogonal, i.e.

$$\mathbf{S}^\dagger\mathbf{S} = M\mathbf{I} \tag{9}$$

with $\mathbf{I}$ being an identity matrix, and balanced, i.e.

$$\mathbf{S}^\dagger\mathbf{1} = \mathbf{0} \tag{10}$$

with $\mathbf{0}$ being a vector of all zeros. The channel transfer function is estimated as a vector $\hat{\mathbf{g}}_l$, obtained in a least-squares sense as

$$\hat{\mathbf{g}}_l = \frac{1}{M}\mathbf{S}^\dagger\mathbf{r}_l, \tag{11}$$

where $\mathbf{S}^\dagger$ represents the conjugate transpose of $\mathbf{S}$.

C. Performance Metrics for Code Selection

To design an appropriate OCAI scheme, a generalized performance metric that is independent of any particular scene and imaging aperture combination is needed. A viable metric is 1/NMSE, where NMSE is the normalized mean squared error of the channel estimations $\{\hat{\mathbf{g}}_l\}$ which is defined as

$$\text{NMSE} = \frac{\mathrm{E}\left\{(\hat{\mathbf{g}}_l - \mathbf{g}_l)^\dagger (\hat{\mathbf{g}}_l - \mathbf{g}_l)\right\}}{\mathrm{E}\left\{\mathbf{g}_l^\dagger\mathbf{g}_l\right\}}, \tag{12}$$

with $\mathrm{E}\{\cdot\}$ being the expected value operator. Note that the symbol-energy-to-noise-spectral-density ratio E_s/N_0 is given by $E_s/N_0 = 1/\sigma_\nu^2$, with $|s_{i,k}| = 1$ and σ_ν^2 being the measurement noise variance.

III. OCAI PERFORMANCE ANALYSIS

The performance of the proposed OCAI scheme was first analyzed using numeric simulations. The used codes belong to the family of Hadamard codes obtained from the columns of Hadamard matrices [22], [23] with $s_{i,k} \in \{-1, +1\}$, forming a binary phase shift keying (BPSK) modulation of the illuminating tones. Unless stated otherwise, a simulated number of TXs $K = 24$ and the code length $M = 32$ were used. To simulate various channels, the amplitudes of the simulated channels $\{\mathbf{g}_l\}$ were chosen to be Weibull distributed [24] with shape parameter $k = 1.8$ and scaling parameter $\lambda = (\Gamma(1 + 2/k))^{-1/2} \approx 0.975$ so that $\mathrm{E}\left\{|G_{k,l}(j\omega)|^2\right\} = 1$ [25]. The channel phases were chosen to be uniformly distributed in the interval $[0, 2\pi)$. Any DC offsets $\{d_l\}$ were initially set to zero, unless noted otherwise.

A. Code Length and Number of Transmitters

Fig. 2 shows the dependence of 1/NMSE on the code length M for $K = 3$ TXs. It can be seen that, with increasing M, the 1/NMSE increases from 1/NMSE = 106 dB for $M = 4$ to 1/NMSE = 115 dB for $M = 32$ in the $E_s/N_0 = 100$ dB case. Also, the coded 1/NMSE is always above its respective single TX case without any coding (dashed lines in Fig. 2 - Fig. 6), e.g., 1/NMSE = 100 dB in the $E_s/N_0 = 100$ dB case. This is due to the additional coding gain as the measurement noise is averaged over the M measurements such that the estimation variance $\sigma^2 = \sigma_\nu^2/M$ is identical to the NMSE [as can be see in (12)].

In Fig. 3, the 1/NMSE as function of the number of TXs is shown. Note that the chosen code length was $M = 32$, regardless of how many TXs were used. As can be seen,
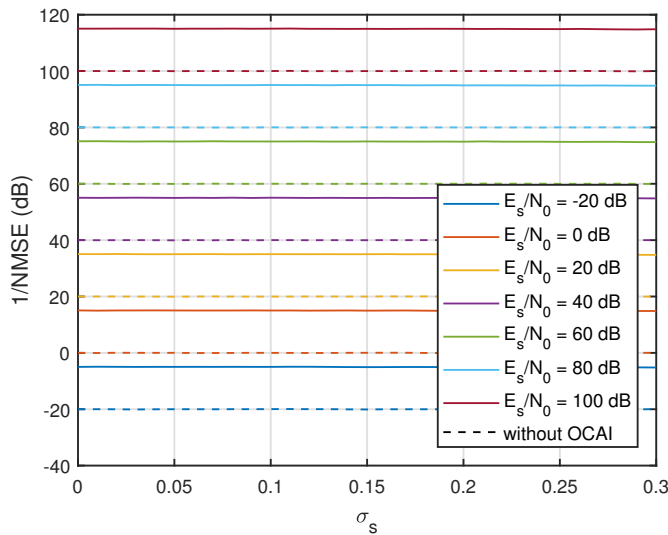
Fig. 4. Comparison of the 1/NMSE performance with and without OCAI as a function of code amplitude imbalance for different E_s/N_0 levels.
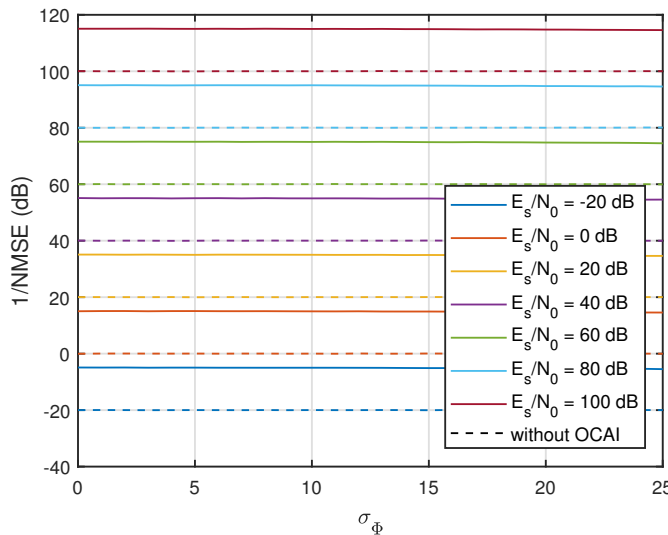

Fig. 6. Comparison of the 1/NMSE performance with and without OCAI as a function of RX DC offset $|d|$ for different E_s/N_0 levels.

Fig. 5. Comparison of the 1/NMSE performance with and without OCAI as a function of of code phase imbalance for different E_s/N_0 levels.

the 1/NMSE is independent of the number of TXs K. For example, 1/NMSE = 115 dB in the $E_s/N_0 = 100$ dB case. This is due to the mutual orthogonality of the different TX codes.

B. Non-ideal Code Realizations

Practical transmitter and receiver hardware will always have some degree of imperfection due to lot-to-lot component variation and temperature variation, among many other factors. From the standpoint of the channel transfer function measurement, this is immediately manifest in gain (amplitude) and phase error in the coded signals. In Fig. 4 and Fig. 5, the effects on the 1/NMSE due to code amplitude and code phase imbalance are illustrated. For these simulations, the code
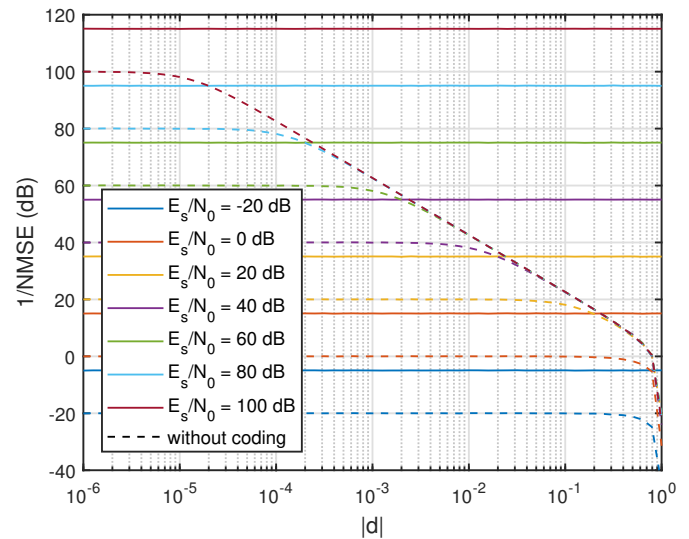
symbols were modified so that the modified code symbols $\tilde{s}_{i,k}$ are given as

$$\tilde{s}_{i,k} = (s_{i,k} + \Delta s_{i,k})e^{j\Delta\Phi_{i,k}}, \tag{13}$$

where $\Delta s_{i,k} \in \{\Delta s_{-1,k}, \Delta s_{+1,k}\}$ represents some code amplitude imbalance and $\Delta\Phi_{i,k} \in \{\Delta\Phi_{-1,k}, \Delta\Phi_{+1,k}\}$ represents some code phase imbalance. As depicted in Fig. 1, it is assumed that the code modulation is performed by a phase shifter such that all the modified $+1$ symbols of a single TX are affected with the same amplitude error $\Delta s_{+1,k}$ and phase error $\Delta\Phi_{+1,k}$, as are all modified -1 symbols with their own respective errors. In the used numeric model, the amplitude and phase imbalance terms are assumed to be zero-mean Gaussian distributed with standard deviations σ_s and σ_Φ, respectively. Practical digital X- and K-band mmW phase shifters are specified to have a root-mean-square amplitude and root-mean-square phase error less than 1 dB (equivalent to $\sigma_s \approx 0.13$) and $5°$, respectively [26]–[28]. Fig. 4 and Fig. 5 show that OCAI is robust to non-ideal code realizations due to practical phase shifters with this level of performance.

C. DC Offset Mitigation

Another important type of impairment often found in low cost, direct conversion receiver hardware is an unwanted, frequency varying DC offset due to internal cross-talk inside the integrated circuits comprising the receiver. Fig. 6 shows the effect of unwanted complex DC offsets $\{d_l\}$ at the receiver output. It can be seen that OCAI is able to mitigate $\{d_l\}$ due to $\mathbf{S}$ fulfilling the balanced property (10). However, the single TX case without any coding is shown to be prone to DC offset induced distortion in the channel estimation. It can be seen that in the $E_b/N_0 = 100$ dB case, the 1/NMSE of the uncoded single TX decreases by 3 dB at $|d| = 10^{-5}$. This is the corner point where the DC offset becomes dominant over the noise ν. For higher levels of $|d|$, the 1/NMSE decreases with the magnitude of the DC offset, i.e. 1/NMSE $= |d|^{-2}$ for $|d| > \sqrt{E_b/N_0}$ and NMSE $= E_b/N_0$ otherwise.
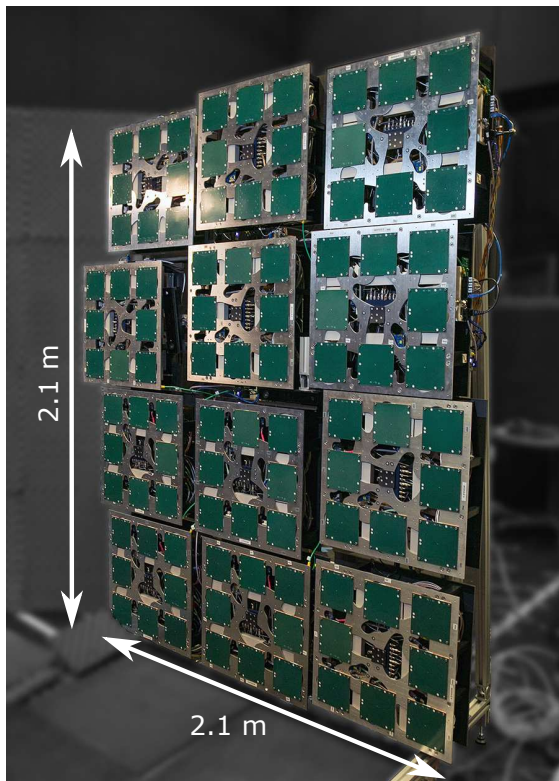
Fig. 7. Metasurface aperture based massive-MIMO mmW imager prototype.

Fig. 8. Photo of one of the 96 printed metasurface apertures and measured pseudo-random radiation patterns as a function of frequency.

Fig. 9. Photo of the resolution test pattern having three different metal strip widths and spacings: 30 mm, 20 mm, and 7 mm.

IV. PROTOTYPE MIMO mmW IMAGER OVERVIEW

The prototype massive-MIMO mmW imager for which this OCAI scheme was developed consists of $L = 72$ RXs and $K = 24$ TXs grouped into twelve identical modules [15], [16]. These modules, arranged on an irregular grid to avoid aliasing effects in the reconstruction, form a 2.1 x 2.1 m metasurface aperture which is able to obtain images in human-scale scenes. The metasurface TX/RX antennas (visible as the 96 green panels in Fig. 7 and in Fig. 8) are planar, printed-circuit based structures. Their inner layer consists of an irregular shaped chaotic cavity feeding horizontal (TX) and vertical (RX) sub-wavelength slot irises that form a Mills-Cross configuration [17]. As shown in Fig. 8, the antenna radiation patterns are strongly frequency-diverse, forming pseudo-random antenna patterns that depend on the frequency of the illumination. The design of these antennas are described in detail in [29]–[32]. This approach results in a frequency dependent backscatter measurement of the ROI that contains spatially encoded backscattered scene information [12].

Each antenna has an associated transmitter or receiver that implements the stepped-FM, massive-MIMO measurement. The radio frequency (RF) range of the imager system is from 17.5 GHz to 26.5 GHz, covering the entire K-band spectrum with $N = 101$ frequency steps and an average system noise floor of -100 dBFS. An OCAI scheme based on Hadamard codes of length $M = 32$ is used. All 24 transmitters and 72 receivers operate in parallel to make the MIMO measurement. The imager obtains $K \times L \times M \times N \approx 5.6 \times 10^9$ measurements per frame with a frame rate of up to 10 Hz. The expected

resolution is 1.6 cm in range and 0.6 cm in cross-range at a distance of 1 m in front of the imager aperture [33].

V. THE MIMO IMAGE RECONSTRUCTION PROBLEM

3D mmW image reconstruction is an inverse problem where frequency dependent measurements of the ROI are used to estimate the reflectivity of the scatterers assumed to comprise the scene. Because MIMO imagers as described in this paper use a sparse sampling of the imager aperture, the inverse problem is typically underdetermined and regularization is needed.

The top level forward model of the MIMO imager is

$$\hat{\mathbf{g}} = \mathbf{H}\boldsymbol{\rho} + \boldsymbol{\nu}, \qquad (14)$$

where $\boldsymbol{\rho} = [\rho_1, \rho_2, \ldots, \rho_N]^T$ denotes the true reflectivity of the scatterers comprising the scene. $\mathbf{H}$ denotes the measurement matrix representing the relationship between the observed measurements $\hat{\mathbf{g}}$ and the scatterers, as described by the signal model of Section II and (1), $\boldsymbol{\nu}$ represents measurement noise. Reconstruction therefore solves for

$$\hat{\boldsymbol{\rho}} = \arg\min_{\boldsymbol{\rho}} \left\{ \|\hat{\mathbf{g}} - \mathbf{H}\boldsymbol{\rho}\|^2 + \lambda \|\boldsymbol{\rho}\|^2 \right\}, \qquad (15)$$

(a) Imager system without OCAI support.

(b) Imager system with OCAI support.

Fig. 10. Reconstructed mmW images of the resolution targets (c.g. Fig. 9) with and without OCAI supported measurements.

which represents a least-squares (LS) approach with a minimum norm solution regularizer. The latter is needed because $\mathbf{H}$ is underdetermined as described above.

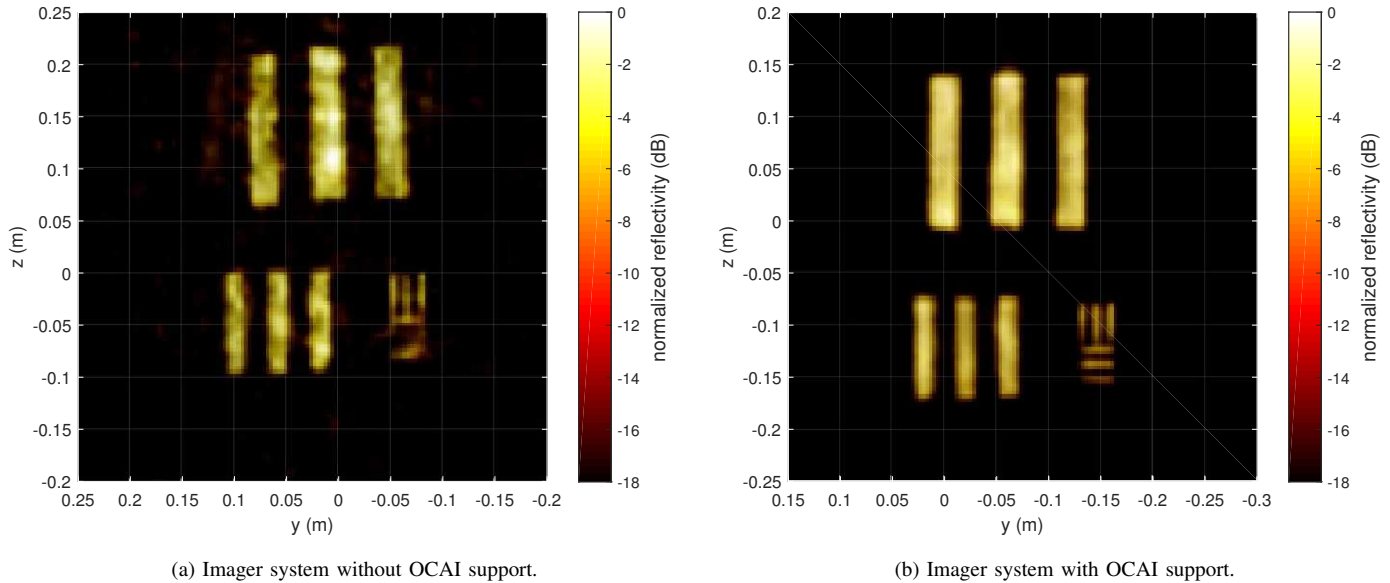To reduce the computational load of the inverse problem, an auxiliary sensor such as the Microsoft Kinect structured-light sensor can be used to reduce the reconstruction volume by avoiding reconstruction of voxels that are known *a priori* to be empty. In the proposed system, a Kinect sensor is used to identify a rectangular volume of interest, which greatly reduces the size of the reconstruction. Given a voxel size of 1.6 cm $\times$ 0.6 cm $\times$ 0.6 cm, the unoccupied voxel data can be used to reduce the number of voxels reconstructed from $\sim138\times10^6$ voxels for a 2 m $\times$ 2 m $\times$ 2 m scene (representing the volume the Kinect is set to observe) to $\sim$200,000 voxels comprising the surface of human-sized targets. In the prototype imager, $\hat{\boldsymbol{\rho}}$ has measurement dimension of $K \times L \times N = 174,528$, enabling reconstruction of the target with reasonable fidelity.

In the computational imaging literature, various approaches have been proposed to address the computational load of the reconstruction problem [34], [35]. Partitioning of the reconstruction to permit hardware acceleration with a graphics processing unit (GPU) offers the potential for significant speed-up relative to CPU based reconstruction [36]–[38]. In this work, a generalized minimal residual (GMRES) algorithm [39], [40] is run on a Intel Core i7-5930K 3.5 GHz CPU with 128 GiB of RAM and four Nvidia GeForce GTX 1080 GPUs. Because of the rapid development of GPU computing and corresponding accelerated reconstruction methods, we refer the reader to these and many other recent works for up-to-date information on the reconstruction problem.

VI. MEASUREMENT RESULTS

To validate the performance of OCAI, measurements and image reconstructions of resolution targets using the massive-MIMO mmW imager introduced in Section IV are compared
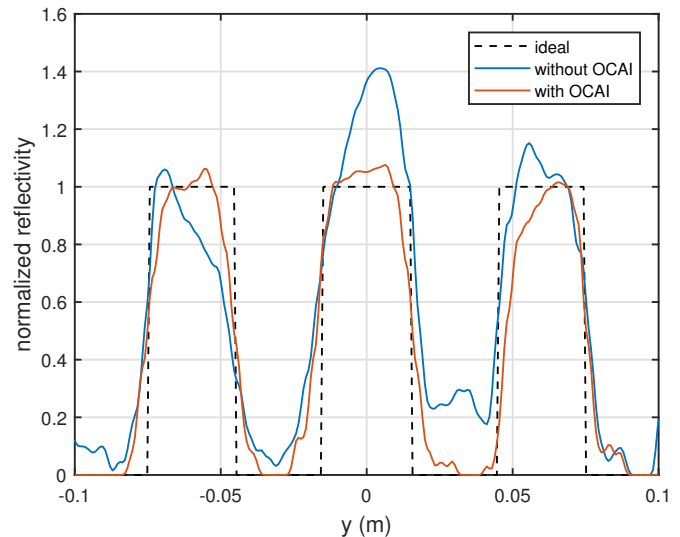
Fig. 11. Measured reflectivity across the three metal strips comprising the 30 mm resolution target (upper half of Fig. 9) with and without OCAI.

to the results of a second imager prototype that does not have OCAI enabled. The latter uses exactly the same metasurface antenna aperture, but measurements are obtained by a single RX/TX pair using a switch-based signal distribution network to sequentially switch through all the different RX/TX antenna combinations [15]. The acquisition frame rate in the OCAI case is 7 Hz, while in the non-OCAI case each frame takes $\sim$ 30 s to acquire due to the non-OCAI sequential acquisition having significant switching speed penalties.

While the improvement in data acquisition speed using OCAI is dramatic (7 Hz with OCAI vs. 0.03 Hz without OCAI), the image reconstruction time can then become the bottleneck in the overall system performance. In this prototype,
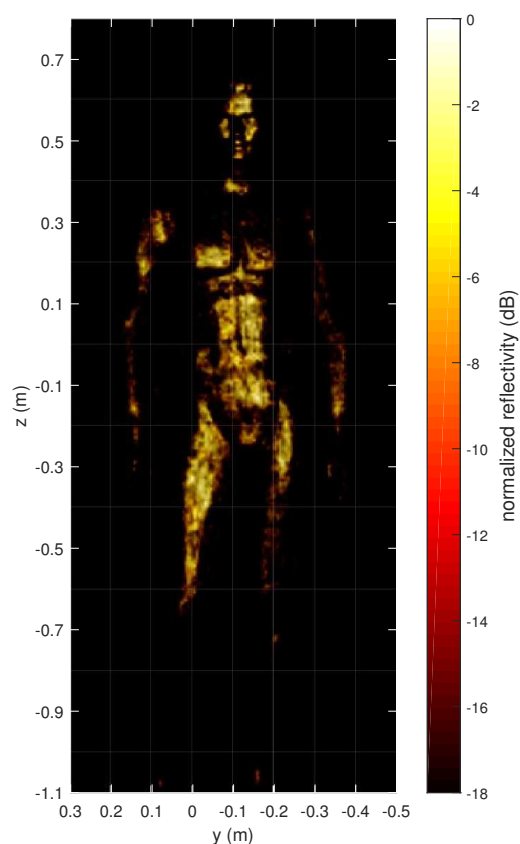
Fig. 12. Reconstructed image of a human-size mannequin using OCAI measurements.

even though data can be acquired at 7 Hz using OCAI, the reconstruction time can be in the range of 150 s to 180 s per frame, depending on the scene size. Note that with alternative reconstruction algorithms that leverage the parallel processing capability of modern GPUs, e.g. [35]–[38], the reconstruction time can be dramatically improved.

Analysis of the image quality improvement enabled by OCAI can be performed by comparing reconstructions of known targets, such as a resolution test pattern. In this work, a resolution test pattern consisting of a series of parallel metal strips with a known width and spacing of 30 mm, 20 mm, and 7 mm (see Fig. 9) was employed. The targets were placed parallel to the imager antennas at a distance of 1 m. Fig. 10 shows image reconstructions (a) without OCAI support and (b) with OCAI support. The image quality improvement due to OCAI is apparent from the visible improvement in image uniformity and shape definition. The useful resolution is also improved as is evidenced by the smallest (7 mm) metal strips being much better resolved.

Fig. 11 presents a quantitative comparison of image quality with and without OCAI. Since the reflectivity of the metal strips comprising the resolution target are known to be nearly unity, the normalized reflectivity across the three metal strips comprising the 30 mm width/spacing resolution target can be used as a measure of ideality in the reconstructed image. As shown in Fig. 11, the reflectivity of the metal strips forming the 30 mm reconstruction target in the upper half of Fig. 9

is assumed to be 1.0 and plotted for reference. As can be seen in the measured images, the reflectivity without OCAI shows substantially larger variation than the reflectivity with OCAI. The corresponding variance of the reflectivity enclosed by the area of the three-strip 30 mm reconstruction target is -16.4 dB without OCAI, but only -23.4 dB with OCAI. Thus, for this resolution target, OCAI is able to reduce the variation in reflectivity by 7 dB.

As a demonstration of the presented imager's ability to produce 3D mmW images of human-scale objects in the ROI, Fig. 12 shows a reconstruction from OCAI based measurement of a conductive paint covered, approximately 2 m tall, full-scale human mannequin. Even very fine details are visible, except at the feet and the shoulders of the mannequin where specular reflection directs energy away from the imager panels. This is an inherent issue for flat-panel mmW imagers due to the specularity of human and metallic targets in the mmW bands; adding some degree of curvature to the imager aperture, or forming composite images from multiple views of the target, are well-known approaches to alleviate this problem.

VII. CONCLUSIONS

This work presents an orthogonal coded active illumination (OCAI) approach for massive-MIMO mmW imagers that is particularly suited to metasurface imaging apertures using low-cost direct conversion receivers. A numerical simulation based design method is presented which shows that the OCAI approach is robust to gain and phase variation in the mmW TX and RX hardware, while additionally mitigating receiver DC offsets common in direct-conversion receivers. These simulations show that the backscatter response estimation error decreases with increasing code lengths, for example, up to 15 dB with codes of length $M = 32$ symbols. This improvement in backscatter response estimation is shown to result in decreased variation in estimated scene reflectivity and thus better apparent image quality.

The OCAI approach was implemented on a 24 TX x 72 RX metasurface aperture based massive-MIMO mmW imager prototype. Validation images of the same resolution test patterns with and without OCAI show that the coding approach improves image quality by reducing measured variation in reflectivity by 7 dB while dramatically improving frame rate from 0.03 Hz (without OCAI) to 7 Hz (with OCAI). A full-size human mannequin is used to demonstrate the achievable mmW image quality. These results suggest that OCAI enabled imagers leveraging metasurface antennas can enable flexible, low cost massive-MIMO mmW computational imaging for a wide variety of active imaging applications.

REFERENCES

[1] I. G. Cumming and F. H. Wong, *Digital Processing of Synthetic Aperture Radar Data: Algorithms and Implementation*. Artech House, 2005.

[2] A. Moreira, P. Prats-Iraola, M. Younis, G. Krieger, I. Hajnsek, and K. P. Papathanassiou, "A tutorial on synthetic aperture radar," *IEEE Geoscience and Remote Sensing Magazine*, vol. 1, no. 1, pp. 6–43, Mar. 2013.

[3] A. Pedross-Engel, C. M. Watts, D. R. Smith, and M. S. Reynolds, "Enhanced resolution stripmap mode using dynamic metasurface antennas," *IEEE Transactions on Geoscience and Remote Sensing*, vol. 55, no. 7, pp. 3764–3772, Jul. 2017.

[4] C. M. Watts, P. Lancaster, A. Pedross-Engel, J. R. Smith, and M. S. Reynolds, "2D and 3D millimeter-wave synthetic aperture radar imaging on a PR2 platform," in *2016 IEEE/RSJ International Conference on Intelligent Robots and Systems (IROS)*, Oct. 2016, pp. 4304–4310.

[5] G. Rankin, A. Tirkel, and A. Leukhin, "Millimeter wave array for UAV imaging MIMO radar," in *2015 16th International Radar Symposium (IRS)*, Jun. 2015, pp. 499–504.

[6] C. Viegas, B. Alderman, J. Powell, H. Liu, H. Wang, and R. Sloan, "Millimeter wave radiometers for applications in imaging and nondestructive testing," in *2015 8th UK, Europe, China Millimeter Waves and THz Technology Workshop (UCMMT)*, Sep. 2015, pp. 1–4.

[7] R. Appleby and R. N. Anderton, "Millimeter-wave and submillimeter-wave imaging for security and surveillance," *Proceedings of the IEEE*, vol. 95, no. 8, pp. 1683–1690, Aug. 2007.

[8] D. M. Sheen, D. L. McMakin, and T. E. Hall, "Three-dimensional millimeter-wave imaging for concealed weapon detection," *IEEE Transactions on Microwave Theory and Techniques*, vol. 49, no. 9, pp. 1581–1592, Sep. 2001.

[9] C. M. Watts, A. Pedross-Engel, D. R. Smith, and M. S. Reynolds, "X-band SAR imaging with a liquid-crystal-based dynamic metasurface antenna," *Journal of the Optical Society of America B*, vol. 34, no. 2, p. 300, Feb. 2017.

[10] R. L. Haupt, *Antenna Arrays: A Computational Approach*. Wiley-IEEE Press, 2010.

[11] G. L. Charvat, L. C. Kempel, E. J. Rothwell, C. M. Coleman, and E. L. Mokole, "An ultrawideband (UWB) switched-antenna-array radar imaging system," in *2010 IEEE International Symposium on Phased Array Systems and Technology*, Oct. 2010, pp. 543–550.

[12] J. Hunt, T. Driscoll, A. Mrozack, G. Lipworth, M. Reynolds, D. Brady, and D. R. Smith, "Metamaterial apertures for computational imaging," *Science*, vol. 339, no. 6117, pp. 310–313, Jan. 2013.

[13] C. L. Holloway, E. F. Kuester, J. A. Gordon, J. O'Hara, J. Booth, and D. R. Smith, "An overview of the theory and applications of metasurfaces: The two-dimensional equivalents of metamaterials," *IEEE Antennas and Propagation Magazine*, vol. 54, no. 2, pp. 10–35, Apr. 2012.

[14] G. Lipworth, A. Mrozack, J. Hunt, D. L. Marks, T. Driscoll, D. Brady, and D. R. Smith, "Metamaterial apertures for coherent computational imaging on the physical layer," *Journal of the Optical Society of America A*, vol. 30, no. 8, pp. 1603–1612, Aug. 2013.

[15] J. N. Gollub, O. Yurduseven, K. P. Trofatter, D. Arnitz, Imani, T. Sleasman, M. Boyarsky, A. Rose, A. Pedross-Engel, H. Odabasi, T. Zvolensky, G. Lipworth, D. Brady, D. L. Marks, M. S. Reynolds, and D. R. Smith, "Large metasurface aperture for millimeter wave computational imaging at the human-scale," *Scientific Reports*, vol. 7, p. 42650, Feb. 2017.

[16] D. R. Smith, M. S. Reynolds, J. N. Gollub, D. L. Marks, Imani, O. Yurduseven, D. Arnitz, A. Pedross-Engel, T. Sleasman, P. Trofatter, M. Boyarsky, A. Rose, H. Odabasi, and G. Lipworth, "Security screening via computational imaging using frequency-diverse metasurface apertures," in *Proc. SPIE*, D. A. Wikner and D. A. Robertson, Eds., vol. 10189, May 2017, pp. 101 890B–1–101 890B–7.

[17] O. Yurduseven, J. N. Gollub, D. L. Marks, and D. R. Smith, "Frequency-diverse microwave imaging using planar Mills-Cross cavity apertures," *Optics Express*, vol. 24, no. 8, pp. 8907–8925, Apr. 2016.

[18] A. Pedross-Engel, D. Arnitz, and M. S. Reynolds, "Self-jamming mitigation via coding for millimeter wave imaging with direct conversion receivers," *IEEE Microwave and Wireless Components Letters*, vol. 27, no. 4, pp. 410–412, Apr. 2017.

[19] J. R. Klauder, A. C. Price, S. Darlington, and W. J. Albersheim, "The theory and design of chirp radars," *Bell System Technical Journal*, vol. 39, no. 4, pp. 745–808, Jul. 1960.

[20] V. T. Vu, T. K. Sjogren, M. I. Pettersson, and H. Hellsten, "An impulse response function for evaluation of UWB SAR imaging," *IEEE Transactions on Signal Processing*, vol. 58, no. 7, pp. 3927–3932, Jul. 2010.

[21] W. L. Melvin and J. A. Scheer, *Principles of Modern Radar, Vol. II: Advanced Techniques*. Edison, NJ: SciTech Publishing, 2013.

[22] S. Georgiou, C. Koukouvinos, and J. Seberry, *Hadamard Matrices, Orthogonal Designs and Construction Algorithms*. Boston, MA: Springer US, 2003, pp. 133–205.

[23] E. Spence, "Classification of Hadamard matrices of order 24 and 28," *Discrete Mathematics*, vol. 140, no. 1-3, pp. 185–243, Jun. 1995.

[24] H. Hashemi, "The indoor radio propagation channel," *Proceedings of the IEEE*, vol. 81, no. 7, pp. 943–968, Jul. 1993.

[25] A. Papoulis and S. U. Pillai, *Probability, Random Variables, and Stochastic Processes*, 4th ed. McGraw-Hill, 2002.

[26] Z. Jin, S. Ortiz, and A. Mortazawi, "Design and performance of a new digital phase shifter at X-band," *IEEE Microwave and Wireless Components Letters*, vol. 14, no. 9, pp. 428–430, Sep. 2004.

[27] A. R. Wolfe and M. E. Davis, "Digital phase shifter elements for a Ku-band phased array radar," in *MTT-S International Microwave Symposium Digest*, vol. 76, Jun. 1976, pp. 347–350.

[28] A. Sharma, A. Kumar, and A. N. Bhattacharya, "A Ku-band 6-bit digital phase shifter MMIC for phased array antenna systems," in *2015 IEEE MTT-S International Microwave and RF Conference (IMaRC)*, Dec. 2015, pp. 404–407.

[29] T. Fromenteze, O. Yurduseven, M. F. Imani, J. Gollub, C. Decroze, D. Carsenat, and D. R. Smith, "Computational imaging using a mode-mixing cavity at microwave frequencies," *Applied Physics Letters*, vol. 106, no. 19, p. 194104, May 2015.

[30] O. Yurduseven, V. R. Gowda, J. N. Gollub, and D. R. Smith, "Multistatic microwave imaging with arrays of planar cavities," *IET Microwaves, Antennas & Propagation*, vol. 10, no. 11, pp. 1174–1181, Aug. 2016.

[31] ——, "Printed aperiodic cavity for computational and microwave imaging," *IEEE Microwave and Wireless Components Letters*, vol. 26, no. 5, pp. 367–369, May 2016.

[32] M. F. Imani, T. Sleasman, J. N. Gollub, and D. R. Smith, "Analytical modeling of printed metasurface cavities for computational imaging," *Journal of Applied Physics*, vol. 120, no. 14, pp. 144 903–1–144 903–14, Oct. 2016.

[33] O. Yurduseven, M. F. Imani, H. Odabasi, J. Gollub, G. Lipworth, A. Rose, and D. R. Smith, "Resolution of the frequency diverse metamaterial aperture imager," *Progress In Electromagnetics Research*, vol. 150, pp. 97–107, 2015.

[34] O. Yurduseven, J. Gollub, H. Odabasi, M. F. Imani, G. Lipworth, A. Rose, P. Trofetter, and D. R. Smith, "Comparison of different reconstruction algorithms for image reconstruction in metamaterial aperture based imaging system," in *2015 9th European Conference on Antennas and Propagation (EuCAP)*, Apr. 2015, pp. 1–5.

[35] D. L. Marks, O. Yurduseven, and D. R. Smith, "Fourier accelerated multistatic imaging: A fast reconstruction algorithm for Multiple-Input-Multiple-Output radar imaging," *IEEE Access*, vol. 5, pp. 1796–1809, Feb. 2017.

[36] S. Devadithya, A. Pedross-Engel, C. M. Watts, and M. S. Reynolds, "Partitioned inverse image reconstruction for millimeter-wave SAR imaging," in *2017 IEEE International Conference on Acoustics, Speech and Signal Processing (ICASSP)*, Mar. 2017, pp. 6060–6064.

[37] ——, "GPU accelerated partitioned reconstruction algorithm for millimeter-wave 3D synthetic aperture radar (SAR) images," in *2017 IEEE International Microwave Symposium*, Jun. 2017, pp. 1983–1986.

[38] S. Devadithya, A. Pedross-Engel, C. M. Watts, N. I. Landy, T. Driscoll, and M. S. Reynolds, "GPU-accelerated enhanced resolution 3-D SAR imaging with dynamic metamaterial antennas," *IEEE Transactions on Microwave Theory and Techniques*, vol. 65, no. 12, pp. 5096–5103, Dec. 2017.

[39] Y. Saad and M. H. Schultz, "GMRES: A generalized minimal residual algorithm for solving nonsymmetric linear systems," *SIAM Journal on Scientific and Statistical Computing*, vol. 7, no. 3, pp. 856–869, 1986.

[40] L. Lars Eldén and V. Simoncini, "Solving ill-posed linear systems with GMRES and a singular preconditioner," *SIAM Journal on Matrix Analysis and Applications*, vol. 33, no. 4, Jan. 2012.

Andreas Pedross-Engel (S'10–M'14–SM'17) received the Dipl.-Ing. degree in electrical engineering and the Ph.D. degree in information and communications engineering from Graz University of Technology, Graz, Austria, in 2009 and 2014, respectively.

From 2008 to 2009 he was with Infineon Technologies Austria AG, were he held the position of a Concept Engineer with focus on signal processing for low-power receiver designs. In 2009 to 2010 he was employed at TeleConsult Austria GmbH as a Research and Development Engineer with the focus on signal processing for global navigation satellite systems (GNSS). From June 2010 to July 2014 he was with the Signal Processing and Speech Communication Laboratory at Graz University of Technology, working as Research Associate toward his Ph.D. degree focusing on nonlinear and mixed-signal processing, design, and modeling of noncoherent ultra-wideband (UWB) receivers. Since November 2014 he has been with the Department of Electrical Engineering at University of Washington, Seattle, WA, USA, working as postdoctoral Research Associate in the area of microwave and mm-wave imaging systems. His research interests include wireless communication and imaging systems, nonlinear- and mixed- signal processing, system characterization and modeling.

Daniel Arnitz (M'11) received the master's degree Dipl.-Ing.(FH) in 2005 from FH Joanneum Kapfenberg, Austria, and a Ph.D. (Dr. techn.) from Graz University of Technology, Austria, in 2011.

He was a PostDoc at the University of Washington, Seattle, WA, USA, and is currently with the Intellectual Ventures Laboratory in Bellevue, WA, USA. His research interests include backscatter channels, microwave and millimeter-wave imaging, wireless power transfer, and RFID localization.

Dr. Arnitz served as General Chair of the IEEE International Conference on RFID (IEEE RFID) in 2016 and as Technical Program Chair of the IEEE RFID conferences in 2012 and 2013.

Jonah N. Gollub (M'16) received the B.A. degree in physics from Reed College, Portland, OR, USA, in 2000, and the Ph.D. degree in physics from the University of California, San Diego, CA, USA, in 2009. His thesis work involved in characterizing the hybridization of metamaterials with magnetic materials.

From 2010 to 2012, he was a Lead Modeling and Simulation Scientist at a startup company developing surface metamaterials with applications targeted toward imaging and biological detection under DARPA, MDA, the Army, and NSF funded efforts. He joined Duke University, Durham, NC, USA, as a Research Scientist in 2013, where he is currently focused on developing real-time millimeter wave imaging approaches which utilize frequency diverse antennas and compressive imaging techniques.

Okan Yurduseven (S'09–M'11–SM'16) received the B.Sc. and M.Sc. degrees in electronics and communications engineering from Yildiz Technical University, Istanbul, Turkey, in 2009 and 2011, respectively, and the Ph.D. degree in electromagnetics from Northumbria University, Newcastle upon Tyne, U.K., in 2014.

He was a part-time Lecturer with the Faculty of Engineering and Environment, Northumbria University, from 2011 to 2014. Since 2014, he has been a Post-Doctoral Associate with the Center for Metamaterials and Integrated Plasmonics, Department of Electrical and Computer Engineering, Duke University, Durham, NC, USA. His research interests include antennas and propagation, antenna measurement techniques, microwave and millimeter-wave imaging, and metamaterials.

Kenneth P. Trofatter received the B.Eng. degree in engineering physics and the B.Eng. degree in computer science from the University of Tennessee, Knoxville, TN, USA, in 2011.

He joined the Center for Metamaterials and Integrated Plasmonics, Duke University, Durham, NC, USA, in 2013 as a Lab Technician, supporting the research and development of novel microwave compressive sensing imaging funded by the DHS. Recently, he has transitioned into graduate study with Duke University to peruse his Ph.D. degree in Electrical and Computer Engineering.

Mohammadreza F. Imani (M'08) received his B.S.E. degree in Electrical Engineering from Sharif University of Technology, Tehran, Iran, in 2007 and the M.S.E. and Ph.D. degrees in Electrical Engineering from the University of Michigan, Ann Arbor, MI, USA, in 2010 and 2013, respectively.

Since 2014 he has been a postdoctoral associate in the Department of Electrical and Computer Engineering, Duke University, Durham, NC, USA. His research includes metamaterials and metasurfaces, microwave imaging and sensing, wireless power transfer, and communication systems.

Timothy Sleasman (S'16) received his B.S. in mathematics and physics from Boston College, Chestnut Hill, MA, USA, in 2013.

Since 2013 he has been working with the Center for Metamaterials and Integrated Plasmonics at Duke University, Durham, NC, USA. He is currently a graduate student in the Department of Electrical and Computer Engineering where he is working toward his Ph.D. degree. His current research interests include computational imaging, dynamically tunable metasurfaces, and novel hardware platforms for generating tailored electromagnetic wavefronts.

Michael Boyarsky (S'17) received the B.S. degree in physics from Boston College, Chestnut Hill, MA, USA, in 2012 and the M.S. degree in mechanical engineering from Marquette University, Milwaukee, WI, USA, in 2014.

Since 2014 he has been with the Center for Metamaterials and Integrated Plasmonics, Duke University, Durham, NC, USA, where he is pursuing the Ph.D. degree in electrical and computer engineering. His research interests include computational imaging, metasurface apertures, and synthetic aperture radar.

Xiaojie Fu (S'15) received the B.S. degree in electrical engineering from Southwest Jiaotong University, Chengdu, China, in 2011 and the M.S. degree in electrical engineering from Southeast University, Nanjing, China, in 2014.

Since 2015 she has been with the Department of Electrical Engineering at University of Washington, Seattle, WA, USA, where she is a Research Assistant and pursuing a Ph.D. degree. Her research interests include microwave and millimeter wave imaging, microwave passive circuit components, and low cost backscatter sensor networks and RF identification (RFID).

Daniel L. Marks received the B.S., M.S., and Ph.D. degree from the University of Illinois at Urbana-Champaign, IL, USA, in 1995, 1998, and 2001, respectively.

From 2001 to 2008, he was a Research Scientist with the Biophotonics Laboratory, University of Illinois at Urbana-Champaign. He is currently an Associate Research Professor with the Department of Electrical and Computer Engineering, Duke University, Durham, NC, USA, where he joined in 2009. His research interests include optics, optical design, computational imaging, millimeter-wave and terahertz imaging, metamaterials, and synthetic electromagnetic structures.

David R. Smith (M'03) received the B.S. and Ph.D. degrees in physics from the University of California at San Diego (UCSD), San Diego, CA, USA, in 1988 and 1994, respectively.

He is currently the Department Chair and James B. Duke Professor of Electrical and Computer Engineering with Duke University and the Director of the Center for Metamaterials and Integrated Plasmonics, Durham, NC, USA. He is an Adjunct Professor with the Physics Department, University of California at San Diego, an Affiliate Faculty Member with the Electrical and Computer Engineering Department, University of Washington, Seattle, WA, USA, and a Visiting Professor of Physics with Imperial College, London, UK. His research interests include the theory, simulation, and characterization of unique electromagnetic structures, including photonic crystals and metamaterials, as well as applications of such materials.

Matthew S. Reynolds (S'01–M'02–SM'10) received the S.B., M.Eng., and Ph.D. degrees from the Massachusetts Institute of Technology (MIT), Cambridge, MA, USA, in 1998, 1999, and 2003, respectively.

He is currently an Associate Professor of electrical engineering and computer science and engineering at the University of Washington, Seattle, WA, USA. He is a cofounder of the RFID systems firm, ThingMagic Inc., the demand-side energy conservation technology firm Zensi, and the home sensing company SNUPI Inc. His research interests include the physics of sensors and actuators, RF identification (RFID), microwave and millimeter wave imaging, and sensor signal processing.